JOURNAL OF MATERIALS SCIENCE 24 (1989) 3647–3659

Structure observations by high-resolution electron microscopy of Ni–B melt-spun alloys (B < 30 at %)

J. AJAO, S. HAMAR-THIBAULT
I.N.P. Grenoble, ENSEEG, LTPCM (UA29), BP75 Domaine Universitaire, 38402 Saint Martin d'Heres, France

J. THIBAULT-DESSEAUX
C.E.N. Grenoble, Departement de Recherche Fondamentale Service de Physique, 85X-38041 Grenoble Cedex, France

The microstructure of a series of Ni–B alloys (15 at % < B < 30 at %) rapidly quenched by melt spinning has been investigated by means of conventional transmission and high-resolution electron microscopy (HREM), and analysed by electron energy loss spectroscopy (EELS) adapted on a scanning transmission electron microscope. A metastable phase is observed in the composition range 21 to 28 at % B where the orthorhombic Ni_3B phase (a = 0.44 nm, b = 0.52 nm, c = 0.66 nm) is expected. High-resolution electron microscopy images of Ni–25 at % B rapidly quenched indicate that a two-phase structure is observed. A metastable phase is observed with a periodicity of 1.0 nm. HREM images and EELS analyses led us to propose the structure of this metastable phase. This phase (Ni_5B_2) is correlated with the monoclinic Hägg carbide Fe_5C_2. Depending on the velocity of the substrate and on the boron concentration, a variety of microstructures has been observed from a faulted to a semi-amorphous structure. The structures are related to the solidification behaviour and the heat flow in the undercooled melt. Particular attention was paid to the eutectic Ni–Ni_3B composition.

1. Introduction

Hardfacing is an important feature in all problems of wear and corrosion [1, 2]. For many uses, the alloys must show good wear and corrosion-resistant properties. The nickel-based hardfacing alloys are characterized by a dispersion of several kinds of hard phases (borides, carbides and silicides).

Various aspects of these alloys have been investigated by different authors, but the solidification behaviour of these alloys have been rarely studied. The autofluxing properties of nickel hardfacing alloys make these alloys interesting for some industries (chemical and glass industries). In spite of numerous studies, only a few works report microstructural and microscopic features [1, 3]. The wear resistance is directly connected to the relations between the matrix and the hard phases: the nature (boride, silicide, carbide), distribution, dimensions and orientation relationship between the phases. Among the eutectics present in these alloys, the Ni(α)–Ni_3B eutectic is very common.

Fig. 1 shows the equilibrium diagram proposed in the nickel-rich region [4]. Table I gives the crystallographic data for the binary stable Ni–B phases [5, 6]. Kolomytsev [7] confirmed the existence of the boride Ni_3B. This boride has been prepared synthetically and electrochemically separated from binary alloys containing more than 0.03 at % B by Kolomytsev [7]. Rundqvist [8] obtained X-ray diffraction data and showed that the lattice of the boride is isomorphous with the cementite lattice (type Fe_3C) and belongs to the space group Pbnm.

In fact, there are some controversial points in the equilibrium diagram of the binary system Ni–B between the different authors. The main difference is the possibility of a metastable eutectic Ni(α)–Ni_2B at 986° C proposed by Schöbel and Stadelmaier [9] and later confirmed by Knotek and Lugscheider [1]. This phenomenon was interpreted by a simple supercooling of these alloys in the works of Portnoi *et al.* [4] and Sobolev and Fedorov [10].

Moreover, the present authors have recently performed a series of investigations on the structure of Ni–B alloys slowly cooled by differential thermal analysis [11]. They have found that some alloys undergo transformation during cooling due to the supersaturation of the liquid in boron, and the formation of metastable phases by rapid quenching cannot be overruled. The Ni–B alloys (18 at % < B < 30 at %) have also been quenched into the glassy state from the melt by different authors [12].

This stimulated us to examine more deeply the solidification behaviour of Ni–B alloys in the composition range 16 to 30 at % B. The influence of cooling rate was also investigated. The study was undertaken by means of conventional transmission electron

0022–2461/89 $03.00 + .12

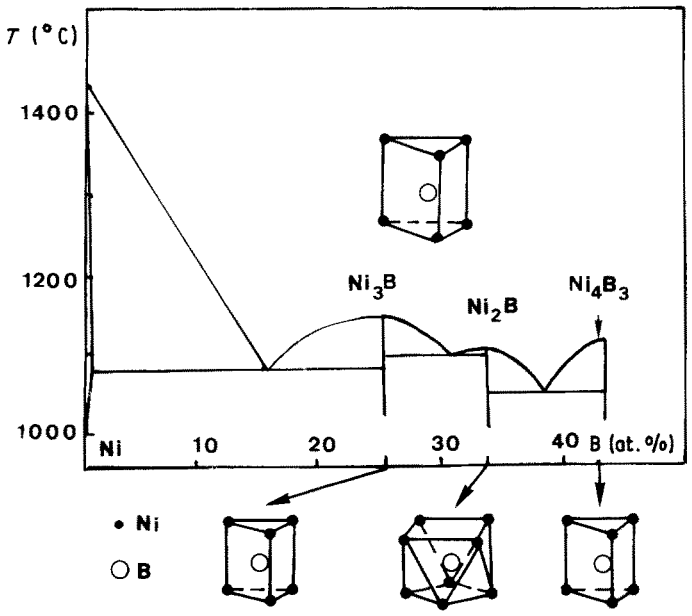

Figure 1 Ni–B equilibrium diagram in the nickel-rich region and local boron environment in crystalline compounds and glasses.

microscopy (TEM), high-resolution electron microscopy (HREM) and electron energy loss spectroscopy (EELS).

2. Experimental procedures

2.1. Samples preparation

A series of alloys from 16 to 30 at % B were prepared. All the alloys observed in this study were produced by the melt-spinning technique which consists of induction melting the accurately weighed mixtures of pure metal (nickel) and nickel boride (NiB) in a crucible with a nozzle (diameter = 0.8 mm) through which the molten alloy is ejected on to a rotating cooled copper surface under an ambient pressure of about 200 mbar helium. The temperature of the liquid alloy before ejection on to the rotating cooled copper surface is kept at about 1250° C. The wheel surface velocity used in this work varied from 15 to 45 m sec^{-1}. The ejection gas pressure was 200 mbar. The ribbons were 1 to 2 mm wide and 30 to 50 μm thick. The cooling rate was estimated to be between 2 and 5 $\times$ 10^5 K sec^{-1}. The value of the heat transfer coefficient (h) between the melt and the copper substrate of 10^5 W K^{-1} m^{-2} has been previously calculated for this apparatus [13]. This value corresponds to a Newtonian thermal transfer.

2.2. Characterization of the ribbons

The structure of the alloys and the nature of the phases were examined by X-ray diffraction (XRD) and transmission electron microscopy performed on thin foils. Thin foils were thinned electrolytically in an electrolyte containing 9/1 acetic/perchloric acid solution at room temperature under 15 V and examined in a direction vertical to the ribbon surface.

In addition to the general observations and microdiffraction analyses in TEM mode, energy-dispersive X-ray analyses (EDX) and electron energy loss spectra were obtained with a VG spectrometer mounted on a VG-HB5-STEM. EDX analyses were obtained on STEM-VG-HB5 with a resolution of 1.5 nm at the sample level. The EEL spectra (pulse counting mode) were recorded using a TRACOR TN2000 multichannel system, which is programmed for quantitative light elements analysis such as boron.

HREM observations were made on a JEM200CX. The contrast variations on the image are simply related to the projection of the crystal structure in only restricted conditions: the incident electron beam must be aligned with low-indexed atomic rows in the crystal and the thickness of the crystal must not be too large (< 20 nm). Moreover, the contrast is dependent on the crystal thickness and on the focalization of the microscope [14]. The determination of atomic position requires the comparison of micrographs and computed images under the same experimental conditions. The electron–material interaction is computed by the multislice method [15]. The image is then calculated by introducing microscope experimental conditions.

TABLE I Crystallographic structure of some stable binary Ni–B compounds [5, 6]

Compound	Space group	Lattice parameter (nm)		
		a	b	c
Ni	Fm3m A_1	0.352		
Ni_3B	Pbnm Do_{11}	0.4389	0.5211	0.6619
Ni_2B	14/mcm C_{16}	0.499		0.424
Ni_4B_3 (o)		1.1953	0.2981	0.6569
NiB	14/mcm C_{16}	0.2925	0.7396	0.2966

3. Experimental results

As reported in a previous paper [11], the solidification behaviour of the alloys in the region B < 30 at % of the Ni–B equilibrium diagram (Fig. 1) is complex. This is essentially due to the difficulty of the nucleation of Ni_3B in the presence of nickel. Before presenting the morphology of melt-spun alloys and the crystallography of the borides in this region, we first present the crystalline structure of Ni_3B.

3.1. Crystalline structure of Ni_3B and HREM images

As reported by Rundqvist [8], Ni_3B possesses an

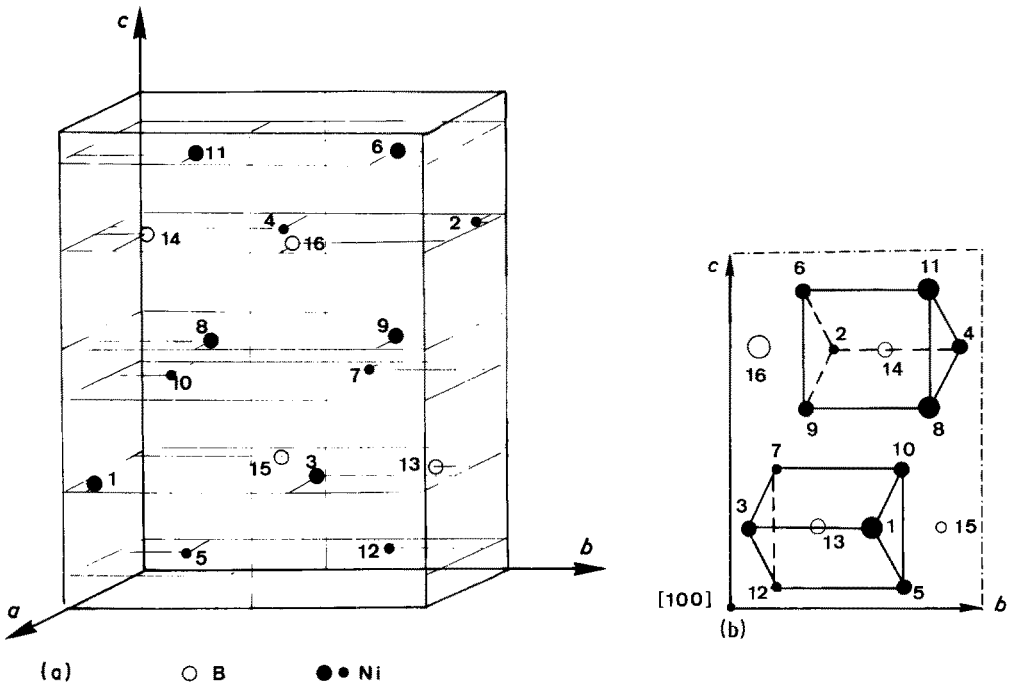

Figure 2 Unit cell of Ni_3B (a) and projection along the [1 0 0] direction showing the prismatic packing of the boron atoms (b).

orthorhombic structure isomorphous with the cementite. Its unit cell contains four motifs of Ni_3B. Its lattice parameters are $a = 0.4389\,nm$ $b = 0.5211\,nm$ and $c = 0.661\,nm$. The structure of Ni_3B belongs to the space group Pbnm. The unit cell is shown in Fig. 2a and the positions of the atoms are presented in Table II. The boron atom occupies the centre of a nearly trigonal prism of nickel atoms as shown in Fig. 2b [5]. The distance Ni–Ni between the nickel atoms lies between 0.25 and 0.264 nm.

It must be noticed that the local environments around a boron atom in Ni_3B and Ni_4B_3 (o) are constructed from a trigonal prism of six nickel atoms while Ni_2B has a boron atom situated in the central hole of an antiprism consisting of eight nickel atoms. In Ni–B glasses [12], the local environment of boron atoms sits in interstices in the same trigonal prism of six nickel atoms.

The images of Ni_3B obtained in HREM along different orientations and the calculated images have been presented previously [16]. As a result of the complexity of the orthorhombic structure of the unit cell of Ni_3B, the correlation between the structure and the images is not direct. The position of the atoms cannot be determined directly from the HREM images but a certain degree of symmetry is conserved between the image and the unit cell. Thus, according to the [0 0 1] direction, the contrast of the images reproduces the rectangular projection of the unit cell on the (0 0 1) plane. In the [1 0 0 direction] the contrast is more complex with a period of $c = 0.66\,nm$. Fig. 3 shows HREM image (a) and the calculated images (d) obtained on the [1 0 0] direction with a focalization of the microscope of $-110\,nm$.

TABLE II Atomic positions in the Ni_3B cell [5]

		x	y	z
Nickel	1	0.864	0.028	0.250
	2	0.136	0.972	0.750
	3	0.636	0.528	0.250
	4	0.364	0.472	0.750
	5	0.347	0.178	0.061
	6	0.653	0.822	0.939
	7	0.153	0.678	0.439
	8	0.847	0.322	0.561
	9	0.653	0.822	0.561
	10	0.347	0.178	0.439
	11	0.847	0.322	0.939
	12	0.153	0.678	0.061
Boron	13	0.433	0.889	0.250
	14	0.567	0.111	0.750
	15	0.067	0.389	0.250
	16	0.933	0.611	0.750

3.2. Morphology of the melt-spun Ni–B ribbons

The sectional view across the thickness of the ribbons shows the existence of either two or three well-distinguished zones. The first zone with finely distributed crystalline equiaxed structure is observed towards the wheel-contact side. The intermediate zone is characterized by a columnar structure growing towards the free surface. Lastly, on the free side of the ribbons, we observe an equiaxed structure. This last zone can be narrower than the other two zones or even, in some cases, absent.

The unetched surfaces of the ribbons show a regular surface on the free side of the ribbons. Moreover, the slightly etched surfaces of the ribbons do not show any distinguishable microstructure on the wheel contact side of the ribbons. However, the ribbons present some interesting microstructure on the free side. For instance, in the Ni–19 at % B alloy ribbon, we can distinguish an acicular structure which occupies the major part of the ribbons.

3.3. Microstructure of the melt-spun Ni–B ribbons

Before the details of our observations on the alloy by

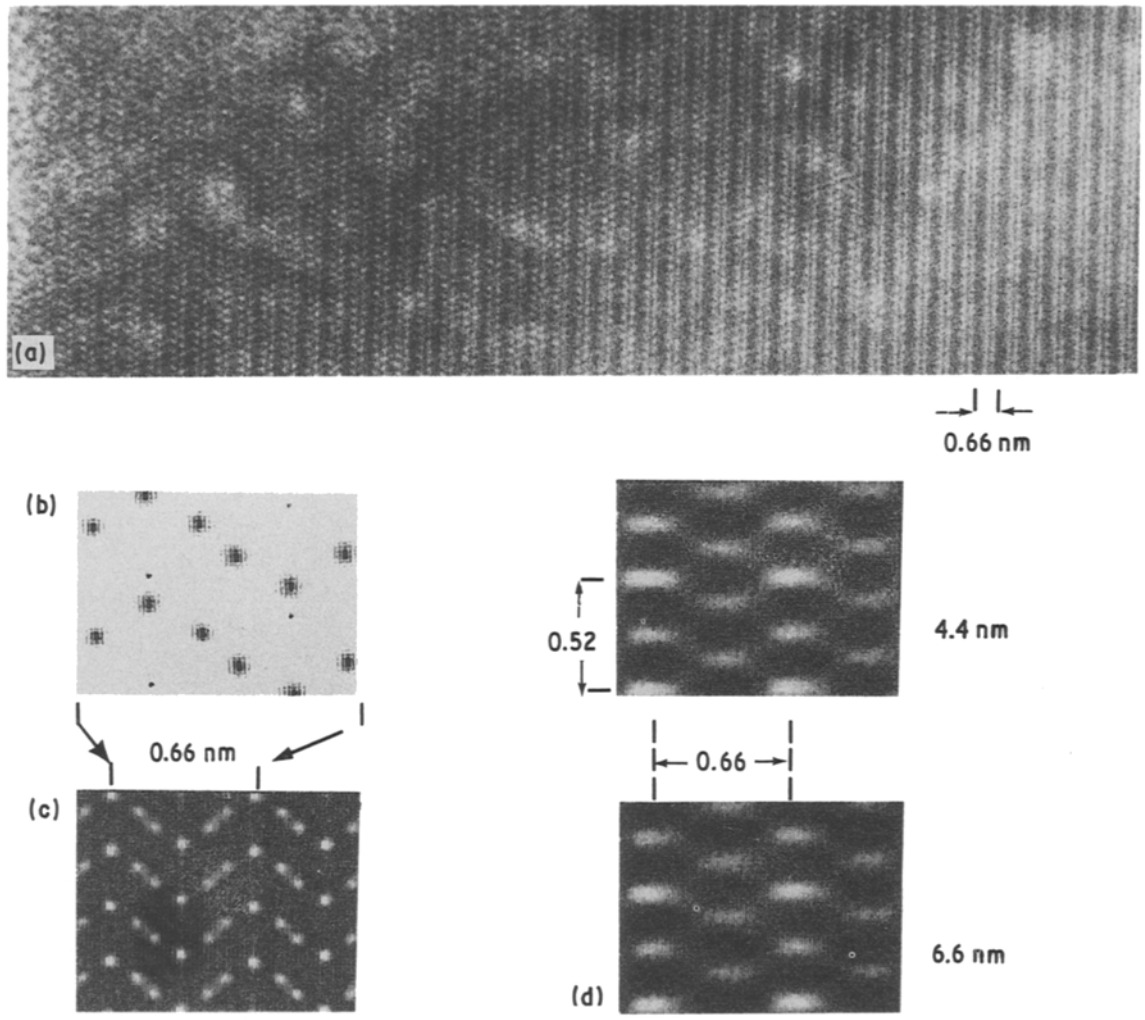

Figure 3 HRE micrograph (a) of Ni_3B (1 0 0) and computed images for different thicknesses (d). The atomic potential (b) and the intensity distribution (c) are also presented. (200 kV, −1100 nm focalization, defocus spread 20 nm, divergence angle of the electron beam 0.005 rd and objective aperture diameter 0.046 nm^{-1}).

alloy study are presented, a summary of the general structure observed in these alloys is given below. Three types of microstructure can be observed on a conventional TEM as a function of the composition of the alloy (Fig. 4) and the rate of cooling:

1. a lamellar eutectic structure; this structure is observed in the ribbons of the alloy with the eutectic composition (Ni–16.2 at % B) melt-spun with a wheel velocity of 15 to 28 m sec^{-1} (Fig. 4a);

2. a needle-like complex structure of Ni_3B; this structure of Ni_3B is observed in alloys with composition between 16 and 19 at % B;

3. a rough globular structure; this structure is observed in the ribbons of the alloys with high boron contents (B > 19 at %) melt-spun with low wheel velocity (V_r = 28 m sec^{-1}) (Fig. 4b and c). This structure is also observed in the melt-spun alloy with eutectic composition but with higher wheel velocity (V_r = 45 m sec^{-1}).

3.3.1. Morphology of the melt-spun Ni–Ni_3B eutectic alloy

The microstructure of the melt-spun alloy (V_r = 15 m sec^{-1}) with the eutectic composition (Ni–16.2 at % B) is shown in Fig. 5a. The eutectic structure remains perfectly lamellar for substrate velocities less than or equal to 28 m sec^{-1} (cooling rate = 10^5 K sec^{-1}). In this range, the higher the cooling rate and the substrate velocity (V_r < 28 m sec^{-1}), the finer the eutectic structure. The two phases making up the lamellar eutectic are perfectly identified as nickel and Ni_3B in X-ray (Fig. 5a) and electron diffractions. For as-cast Ni–Ni_3B eutectic alloy [11], we observed previously that the interlamellar distance is about 0.5 μm and the lamellae of nickel and Ni_3B are approximately the same size. However, in the case of the melt-spun Ni–Ni_3B eutectic alloy, the lamellae have no longer the same size. Thus for the wheel velocity of about 15 m sec^{-1}, the interlamellar distance is about 75 nm, with the lamellae of Ni_3B twice (50 nm) as large as those of nickel (25 nm).

The orientation relationship (Fig. 5b and c) between nickel and Ni_3B phases that we observed in the melt-spun Ni–Ni_3B lamellar eutectic can be described as follows

$$\langle 1\,0\,0\rangle Ni_3B \parallel \langle 2\,1\,1\rangle Ni$$

$$(0\,1\,3)Ni_3B \parallel (1\,1\,1)Ni$$

and

$$(0\,4\,2)Ni_3B \parallel (0\,2\,2)Ni$$

The orientation relationship between the two phases is

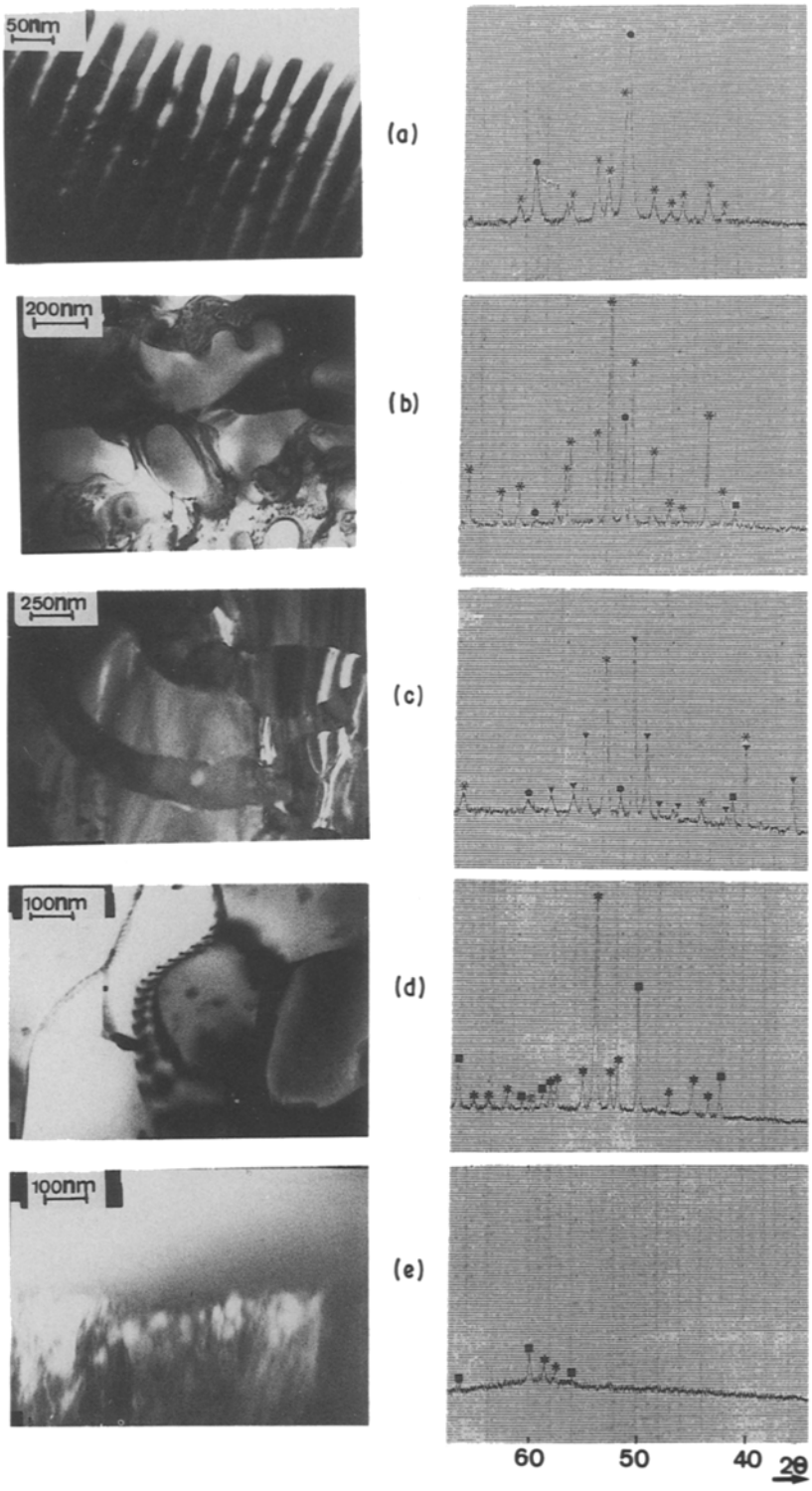

Figure 4 Microstructures of some rapidly cooled Ni–B alloys (V_r = 28 m sec^{-1}) and X-ray diffraction patterns. (a) 16.2 at % B, (b) 21 at % B, (c) 25 at % B, (d) 28 at % B, (e) 30 at % B. (●) Ni, (∗) Ni_3B, (■) Ni_4B_3.

identical to that observed by us in as-cast lamellar eutectic [11]. The direction of the lamellae related to the surface of the ribbon is near the [1 0 0] of Ni_3B.

For higher wheel velocity (V_r = 45 m sec^{-1}), the structure of the eutectic alloy is no longer lamellar but globular consisting of two phases. For intermediate substrate velocities, the structure seems to be the needle-like structure mentioned previously.

3.3.2. Morphology of the melt-spun Ni–19 at % B alloys

The microstructure of the ribbons of this alloy in TEM is, to say the least, complex. The microstructure presented by this alloy depends on the localization of the field of observation in the sample. Thus, the microstructure of the melt-spun alloy is not homogeneous. The following sequence of the structure can be observed in the alloy:

(i) faulted structure which appears in the TEM a lath structure;

(ii) a zone with elongated precipitates of Ni(α);

(iii) then a zone with spherical precipitates of Ni(α).

Our X-ray diffraction analyses, as well as all the electron diffraction patterns obtained in the TEM on this alloy, show only the existence of the two phases nickel and Ni_3B. No other supplementary peaks due to other phases such as Ni_2B can be observed in this alloy.

The lath area seems to be composed of well-oriented

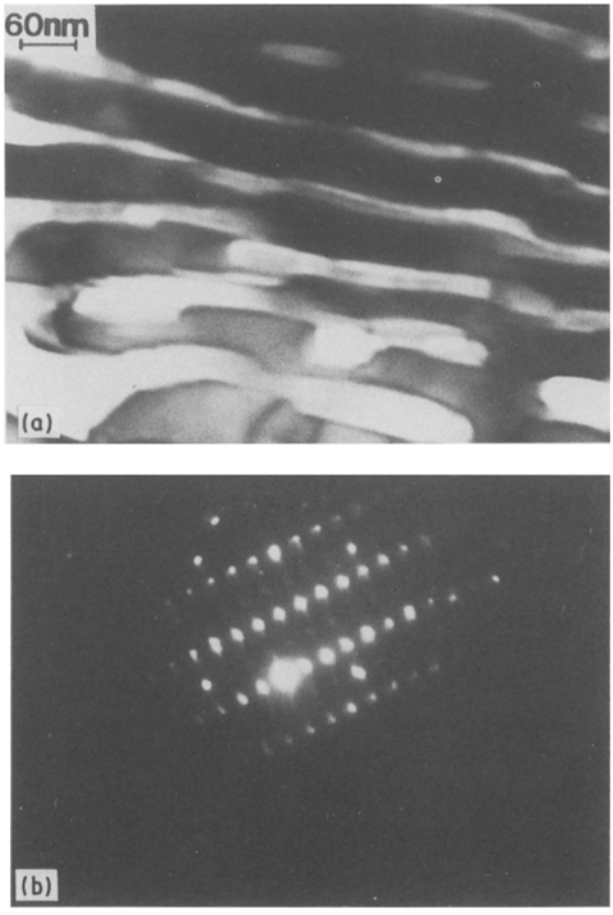

Figure 5 Transmission electron micrograph of Ni–16.2 at % B eutectic alloy rapidly cooled (V_r = 15 m sec^{-1}). (a) Bright field, (b) superposed diffraction pattern, and (c) key diagram.

lamellae of Ni_3B while the zone with elongated precipitates is made up of the two solid phases nickel and Ni_3B. In this region, the size of the lamellae of nickel varies from 50 to 100 nm and they are always smaller than those of Ni_3B (200 nm). In this zone, the size of the nickel precipitates never exceeds 100 nm. These elongated precipitates of nickel are oriented parallel to the laths of Ni_3B. They coarsen and become spherical as one moves away from the central region with the lath structure.

Fig. 6 shows a micrograph (a) and two electron diffraction patterns obtained in the lath regions of Ni_3B in this alloy. These diffraction patterns present, in addition to the spots (1 0 0) and (0 1 0) of Ni_3B indicating an orientation along the [0 0 1] direction, either some diffuse streaks perpendicular to the [1 0 0] direction (b) or even some discrete spots (c) in the same direction.

The corresponding image of the above structure in HREM is shown in Fig. 7. It is pertinent to remark here that the periodicity of the image is about 1 nm which seems to be twice the periodicity of the (0 1 0) plane in Ni_3B. This double periodicity is not easily evident and its observation strongly depends on the focal point of the microscope during the observations. This HREM image shows that there exist some planar defects (arrowed) parallel to the plane of periodicity of 1 nm. It can be observed that this region is not only composed of laths but also of a great quantity of parallel planar defects.

The observation in HREM of the remaining Ni_3B zone in the melt-spun alloy with elongated and spherical precipitates shows that the periodicity of the observed contrast is typically that of Ni_3B with c = 0.66 nm as shown in Fig. 8. The orientation of the orthorhombic structure Ni_3B is [1 0 0] in this area. The b and c axes are in the plane of the ribbon.

3.3.3. Morphology of the melt-spun Ni–21 at % B and Ni–25 at % B alloys

The microstructures presented by the ribbons of these two alloys melt-spun with a wheel velocity of about 28 m sec^{-1} are similar. The microstructure as well as the diffractogram obtained on Ni–21 at % B are shown in Fig. 4b. Two phases are easily distinguished from the micrograph. However, for this alloy, the diffractogram shows the existence of the Ni(α) and Ni_3B phases with some small peaks which can be indexed perhaps as the intermetallic phase Ni_2B. The observations of this alloys at higher magnifications show the existence of precipitates in the nickel interdendritic groove. The EEL spectra obtained on these three different phases as well as a higher magnification micrograph of this alloy are shown in Fig. 9. These spectra show that there exist at least three different phases with different boron levels:

(a) the globular or dendritic phase (1) with an average content of boron (B_k = 188 eV). It is relatively clear and presents little contrast in Fig. 9a.

(b) a second phase (2) external to phase 1, with a very small boron content is identified as the nickel phase, and

(c) the third phase (3) is observed in the internal part of the nickel phase. This phase is in the form of very small, almost spherical, precipitates of about 20 nm. The intensity of the peaks (191, 194 and 198 eV) of the B_k loss is very large. This is characteristic of the fine structure of the compounds very rich in boron [17].

All the diffraction patterns obtained for this alloy are relatively difficult to interpret. Despite this, we are able to observe the presence of these three phases Ni(α), Ni_3B and Ni_4B_3 (o). The last compound diffracts well and corresponds to the small perfectly crystallized precipitates very rich in boron (phase 3).

As mentioned earlier, the morphology of melt-spun Ni–25 at % B alloy is similar to that of the Ni–21 at % B melt-spun with the wheel velocity V_r =

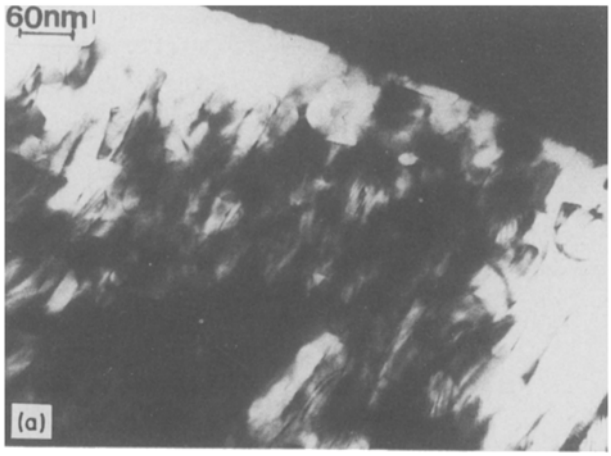

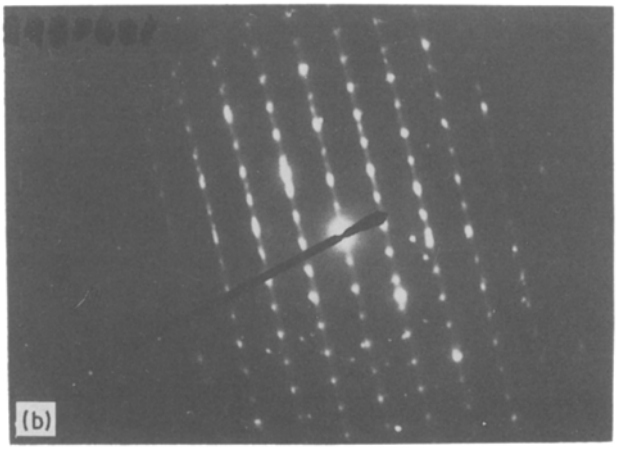

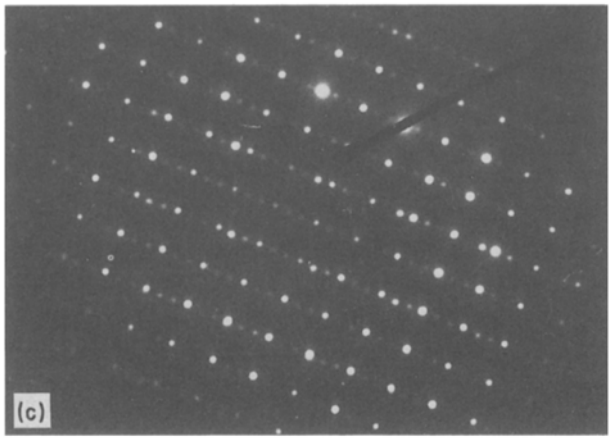

Figure 6 Ni–19 at % B melt-spun alloy. TEM observations of the structure (a) showing two diffraction patterns with elongated (b) and discrete (c) spots.

28 m sec^{-1}. The microstructure and the X-ray diffractogram obtained on the melt-spun Ni–25 at % B alloy are shown in Fig. 4c. On the micrograph, as in the Ni–21 at % B alloy two interconnecting phases can be visualized. However, the X-ray diffraction peaks show the presence of at least three phases, nickel, Ni_3B and Ni_4B_3 (o) with some traces of Ni_2B. As in the Ni–21 at % B alloy, the same three phases are analysed in EELS.

An interface between the two major phases (1 and 2) obtained by HREM is shown in Fig. 10a. Contrary to previous observations on as-cast Ni–Ni_3B eutectic [11], the nickel phase (2) is extremely magnetic and observations of the (1 1 1) planes was not possible. Moreover, the structure of the second phase reveals some complexity. The image shows a contrast of periodicity of 1 nm, which does not correspond to any recticular distances of Ni_3B (Fig. 10b). Contrary to our observations in the Ni–Ni_3B interface in the as-cast lamellar eutectic alloy, the interface between phases 1 and 2 is not well-defined, even though certain planar portions can be observed.

Ageing of these two alloys at temperatures between 500 and 600° C for 1 h shows that this complex structure is stable up to 600° C. Heat treatments performed

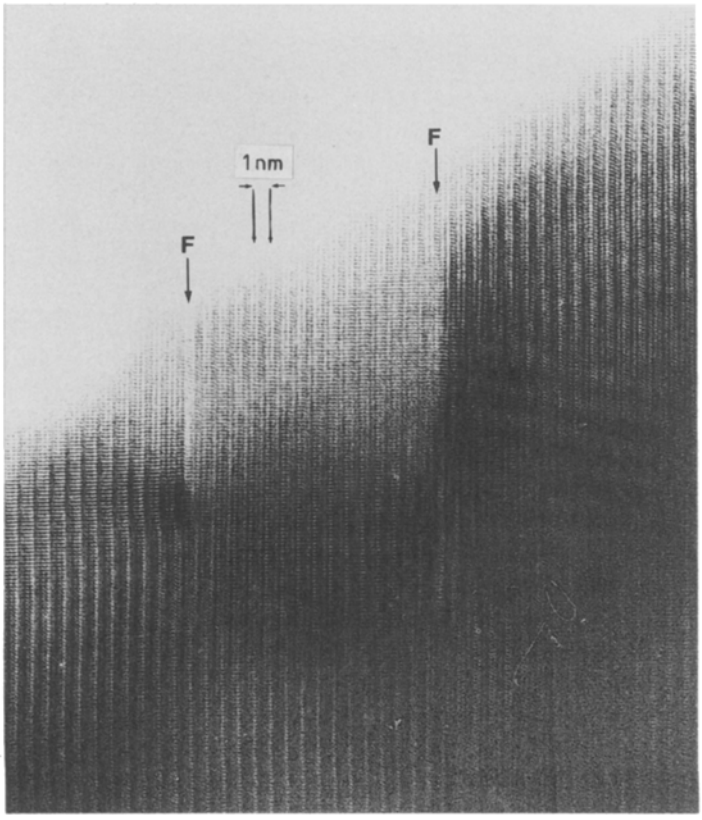

Figure 7 Ni–19 at % B melt-spun alloys (V_r = 28 m sec^{-1}). HRE micrograph obtained in the zone showing a periodicity of 1 nm.

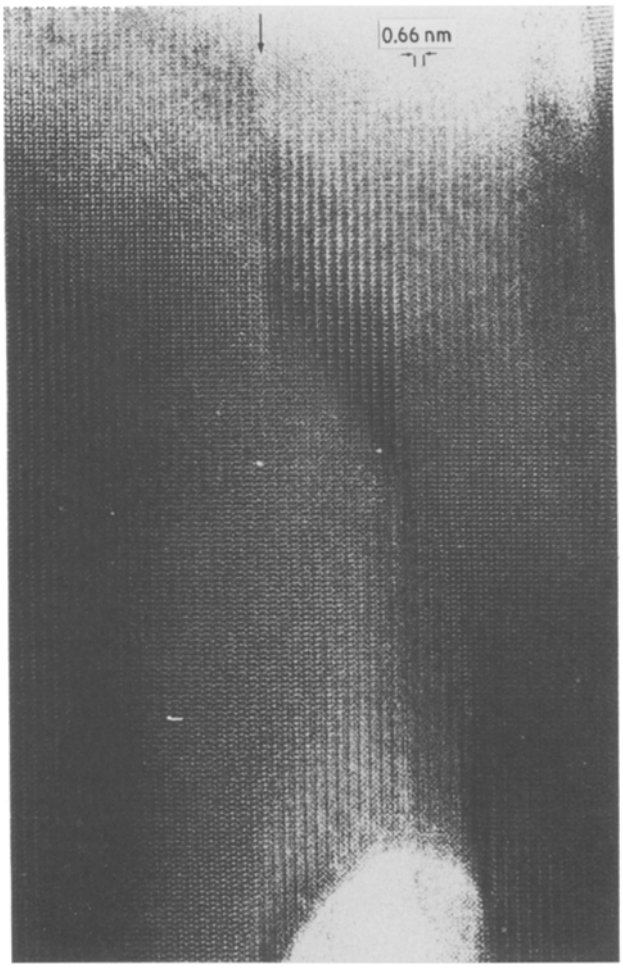

Figure 8 Ni–19 at % B melt-spun alloys (V_r = 28 m sec^{-1}). HRE micrograph obtained in the zone showing a periodicity of 0.66 nm.

above 600° C transform the two-phase alloys into a single-phase structure of Ni_3B. All electron diffraction patterns obtained on melt-spun Ni–25 at % B alloy heat treated above 600° C for 1 h are well-indexed as the Ni_3B orthorhombic phase.

The major part of the microstructure of the melt-spun Ni–25 at % B alloy, quenched with a lower wheel velocity (V_r = 15 m sec^{-1}), is made up of the lath structure as previously mentioned in Ni–19 at % B alloy quenched at higher velocity. The electron diffraction patterns are equally characterized by diffuse streaks due to defects.

3.3.4. Morphology of the melt-spun Ni–28 at % B and Ni–30 at % B alloys

The melt-spun Ni–28 at % B alloy, quenched with the wheel velocity of 28 m sec^{-1}, presents a uniform single-phase structure with grains more or less equiaxed. Columnar grains can equally be observed depending on the localization within the sample. Most of the electron diffraction patterns are very difficult to index. Our experimental analyses by EELS show a structure of uniform composition. No variation in boron concentration can be observed from grain to grain. However, the intensities obtained in X-ray diffraction cannot be attributed to only one phase such as Ni_3B or Ni_2B (Fig. 4d).

In the case of Ni–30 at % B alloy, two principal types of structures are evident; a lath structure and an amorphous structure (Fig. 11). The interface between the two structures is made of steps more or less regular parallel to the lath structure. The microcrystallized region presents a large number of defects. The EELS performed on this alloy show that the amorphous zone (A) is made of a uniform composition of boron. However, in the microcrystallized zone, two types of lamellae with different boron concentrations can be visualized. The lamellae with clear contrast (2) are revealed as richer in boron content than those with dark contrast (1) as shown on the EEL spectra of Fig. 11.

4. Discussion

Two points are to be discussed: the nature and domain of stability of the metastable phase, then the relation between the solidification behaviour during melt-spinning and microstructure of the ribbons in the domain of stability of the metastable phase and the eutectic composition.

4.1. Characterization of the metastable phase, χ

First of all, a brief summary will be given of the different structures observed in the melt-spun alloys with compositions 16 at % < B < 30 at %. Two types of structures were observed.

1. An acicular structure surrounded by two zones made up of elongated and spherical precipitates. This structure is observed in the melt-spun Ni–19 at % B alloy. At higher magnification, the acicular structure appears in the form of a solid solution but with a contrast of periodicity (1 nm) twice that of the Ni_3B phase (Fig. 7). However, the zones with the nickel precipitates show a contrast of periodicity c = 0.66 nm equal to that of the orthorhombic phase of Ni_3B (Fig. 8);

2. A globular dendritic structure which is observed in the melt-spun Ni–21 at % B and Ni–25 at % B alloys. The first phase is nickel and another phase in the form of a solid solution is observed. This last phase in HREM shows a contrast of periodicity of 1 nm (Fig. 10) which is analogous to the one mentioned above.

Moreover, the boron content (EELS) of this χ phase (1 in Fig. 9) is small in the range 25 to 30 at % B as in Ni_3B. This boron content is much lower than that observed in the orthorhombic phase of Ni_4B_3 (phase 3). This χ phase appears with periodicity of 10.5 nm. The lattice parameters in the two other directions are in the neighbourhood of that of Ni_3B. None of the stable phases (Ni_3B, Ni_2B or Ni_4B_3) (Table I) in the Ni–B system fulfils all the conditions stated above.

4.1.1. Nature of the metastable phase, χ

Among the metastable phases in the Ni–B system, is the cubic τ ($Ni_{23}B_6$) phase of the $Cr_{23}C_6$ type mentioned by different authors in melt-spun Ni–B–Si alloys [18]. We did not consider this phase for two reasons:

(i) its boron content (= 0.20) is too low to give rise to this phase;

(ii) this τ phase can easily be observed and indexed

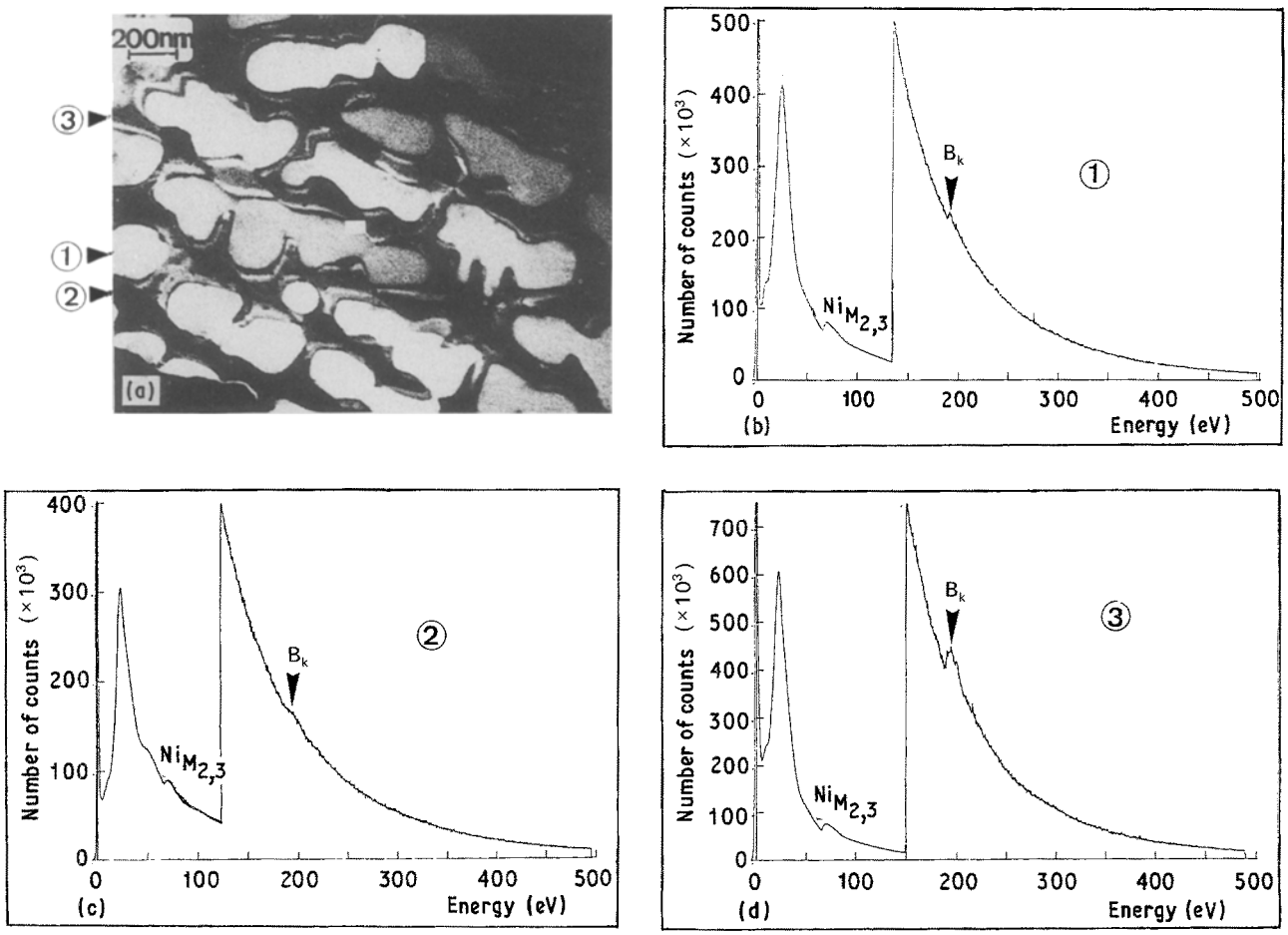

Figure 9 Ni–21 at % B rapidly quenched (V_r = 28 m sec^{-1}). Energy loss spectra showing Ni_{M2-3} and B_k shells in nickel (2), in the χ (1) phase and in the precipitates (3).

as shown in a previous paper [11] in the case of small additions such as titanium.

Therefore, the possibility of a new structure will be examined in the following discussion and the proposed structure of the metastable phase will be considered with a reasonable explanation from the crystallographic point of view. The Ni_3B phase being isomorphous with the cementite Fe_3C (a = 0.452, b = 0.5089 and c = 0.6744 nm), we then directed our investigations towards the carbides.

The iron-rich carbides of $Fe_{2n+1}C_n$ ($1 < n < 5$) types have been particularly studied [19]. These structures consist of the metastable compounds of the type Fe_5C_2, a structure which can be derived from the Fe_3C orthorhombic structure formed from layers of prisms (Fig. 12a) made up of six atoms of iron surrounding an atom of carbon. The six atoms of iron are arranged in the form of a prism with two triangular bases. This Fe_3C structure can be described as pleated metal atom layers formed of a stacking of layers of prisms parallel to the (1 0 0) plane and comprising two types of iron atoms: FeI placed at the peak of the prism, and FeII placed in the rectangular base of the prism (Fig. 2b).

The structure of Fe_5C_2 is monoclinic and the lattice parameters are a = 1.1562 nm, b = 0.4573 nm, c = 0.5058 nm, β = 97°44′ [20]. This structure can be

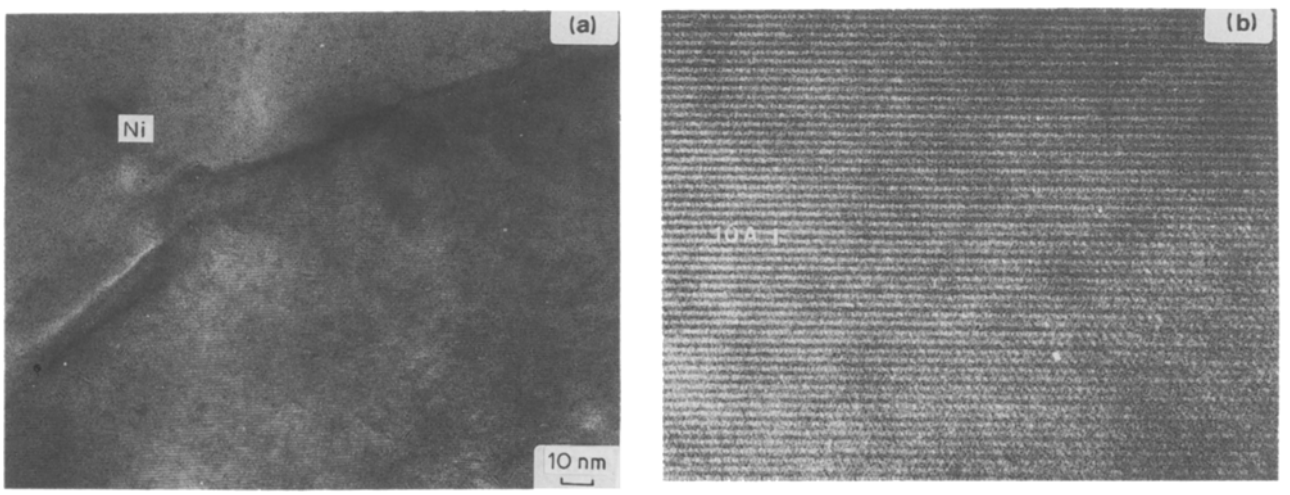

Figure 10 Ni–25 at % B rapidly quenched (V_r = 28 m sec^{-1}). (a) High-resolution electron micrograph of an interface between nickel and the χ phase. (b) Higher magnification on the χ phase showing a periodicity of 1 nm.

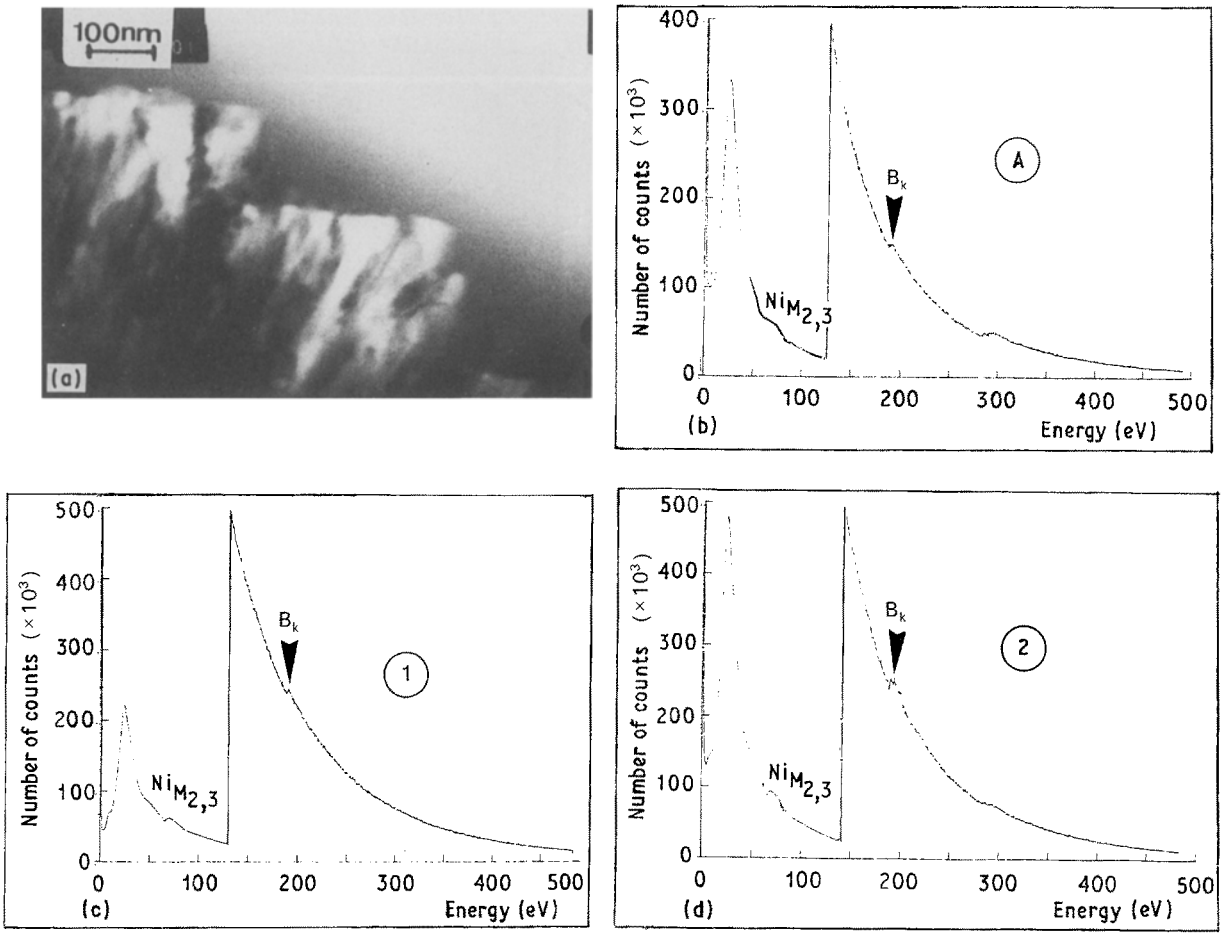

Figure 11 Ni–30 at % B rapidly quenched (V_r = 28 m sec^{-1}), showing a sharp interface between the amorphous (A) and crystalline zones. Energy loss spectra showing Ni_{M2-3} and B_k shells in the two phases (1, 2) of the eutectic.

described as a double-layer of prisms similar to those of the Fe_3C phase (Fig. 12a) but with three different types of iron atoms (Fig. 12b). From the near equality of the two lattice parameters, it is obvious that the two compounds are structurally related. These strong structural analogies between Fe_3C and Fe_5C_2 allow the possibility of passage from one structure to the other.

Among the borides, it is necessary to remark that the two compounds Pd_3B orthorhombic (a = 0.485 nm, b = 0.546 nm, c = 0.757 nm) and Pd_5B_2 monoclinic (a = 1.279 nm, b = 0.495 nm, c = 0.547 nm, β = 97°4′) exist [5]. In addition, the palladium element belongs to the same column VIII as the nickel element in the Periodic Table. This stimulated us to examine the possibility of the existence of the compound Ni_5B_2 in the Ni–B system with a monoclinic structure and lattice parameters a = 0.439 nm, b = 0.520 nm, c = 1.050 nm, α = 97°. Several arguments are in favour of the existence of such a phase.

1. The boron content (0.28) of the Ni_5B_2 phase is only slightly higher than that measured (0.25) in the Ni_3B phase; thus the development of a double-phased

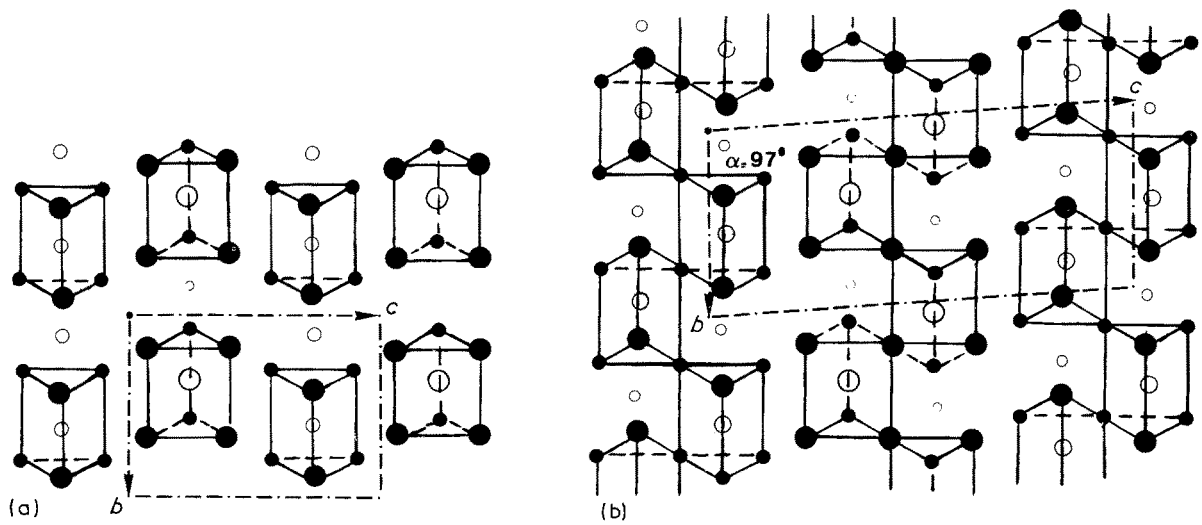

Figure 12 Projections along the a-axis for (a) Fe_3C and (b) Fe_5C_2 showing the crystallographic relation between the two phases.

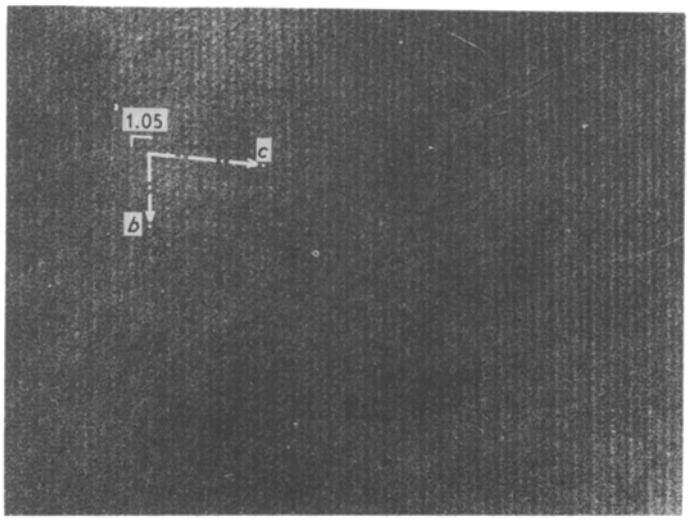

Figure 13 Ni–25 at % B rapidly quenched (V_r = 28 m sec^{-1}). High-resolution electron micrograph on the χ phase showing a periodicity of (*c*) ~ 1 and (*b*) 0.52 nm.

structure between Ni_5B_2 and nickel is possible during quenching of the Ni–25 at % B alloy composition (Fig. 10).

2. In the rapidly quenched Ni–28 at % B alloy (Section 3.4) the X-ray diffraction patterns can be effectively indexed with the monoclinic Ni_5B_2 structure and this result agrees with EELS results showing a homogeneous composition.

3. Deeper observations in HREM of some zones of this Ni_5B_2 phase show that in addition to the contrast of periodicity of 1 nm, a contrast can be equally observed formed with the axes: b = 0.52 nm and c = 1.05 nm and an angle of 97° as shown in Fig. 13 corresponding to the projection along the [1 0 0] axis. This projection is comparable with that shown in Fig. 12b.

Furthermore, as reported above, the passage from the Fe_3C to Fe_5C_2 structure starts from the plane defects in the (0 0 1) plane of Fe_3C. We have effectively observed some planar defects in the Ni_3B (Fig. 8) as well as in the Ni_5B_2 phase (Fig. 7) perpendicular to the plane formed by a and b, even in the zone where the Ni_3B phase is perfectly crystallized. These faults in Ni_5B_2 phase are parallel to the primitive phase (0 0 1) of the Ni_3B phase. These faulted zones correspond to the needle-like structure observed in the melt-spun Ni–19 at % B alloy (Fig. 6).

The Ni_3B and Ni_5B_2 zones are always well separated. We never observed mixing of Ni_3B and Ni_5B_2 in the same area, as is sometimes observed in the Fe_3C–Fe_5C_2 system [22].

4.1.2. Existence domain of the Ni_5B_2 phase

Heat treatment was performed at different temperatures in order to obtain the stability domain of this Ni_5B_2 metastable. Fig. 14a shows the stability domain of this phase which extends from 16 to 30 at % B. This phase decomposes at temperatures above 600° C for the stoichiometric composition (Ni–28 at % B). For lower boron levels, the decomposition temperature is lower. Therefore, for the Ni–19 at % B, this temperature is around 450° C. For the eutectic composition (Ni–16.2 at % B), the globular structure is only observed for very high substrate velocities (V_r = 45 m sec^{-1}) and this globular structure remains globular until 300° C.

For higher boron contents (B = 30 at %) the stability domain of glasses is well-evidenced and interferes with the stability domain of Ni_5B_2 as shown in the same figure.

4.2. Solidification behaviour of Ni–B melt-spun alloys

4.2.1. Behaviour in the existence domain of the Ni_5B_2 phase

In order to interpret the structure and the morphologies observed in undercooled specimens, we must take into account the thermal history of the ribbon [23, 24].

Heat flow models of rapid solidification processes show that the cooling rate is not uniform during cooling. It depends on time and on the position in the melt film. Two different models are possible:

(i) the model based on the homogeneous nucleation theory [25], where the fraction solidified in the foil increases with the distance from the substrate; and

(ii) the model based on the heterogeneous nucleation, where the nucleation is caused by the contact of the melt with the substrate [26].

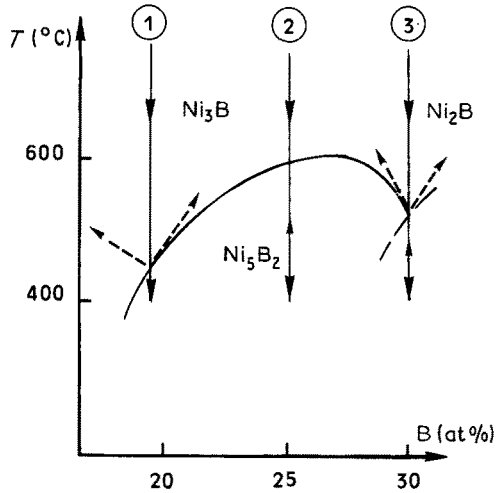

Figure 14 Stability domain of the Ni_5B_2 metastable phase and solidification sequences during melt-spinning for three compositions.

It seems from our observations, that the homogeneous nucleation model can explain the solidification behaviour of these alloys. As previously mentioned, the cooling rate depends on localization in the ribbon; moreover, it depends equally on the temperature interval (T_1–T_2) of homogeneous nucleation for the different phases. Sellger and Löser [27] propose values for the temperature interval of homogeneous nucleation for some analogous systems $Fe_{80}B_{20}$, $Fe_{83}C_{17}$. The temperature intervals for homogeneous nucleation for these two systems are, respectively, 1043 to 869 K and 994 to 784 K. These temperatures are in the same range as the decomposition temperatures (T_d) of the Ni_5B_2 phase.

The rapid solidification on a copper substrate with a Newtonian foil–substrate heat transfer gives rise to different temperature distributions with time and subsequently to different morphologies. Fig. 14b shows a schematic illustration of the solidification paths for three different boron levels.

If the cooling rate is high enough to prevent a large amount of crystallization as the melt passes the temperature interval of homogeneous nucleation, calculated in our case from 750 to 600° C, the ribbon will be amorphous. In our composition and velocity ranges, we never obtained completely amorphous specimens.

If the local cooling rate is not high enough to prevent large amounts of crystallization, the release of latent heat due to the primary crystallization is important, the temperature in the melt increases and the density of nuclei equally increases. Different morphologies can be observed depending on composition. In Ni–30 at % B alloy, we effectively observed a sharp interface between the first amorphous zone and the crystalline material (Fig. 11) which appears as a eutectic phase between the two phases Ni_3B and Ni_2B, as expected from the phase diagram (Fig. 1a).

In the Ni–B alloys with lower boron contents ($19 < B < 28$ at %), the solidification model included both Ni_3B and Ni_5B_2 crystallization in the undercooled melt film. The solidification sequence is described as follows: if the local cooling rate is not too rapid, the fast crystallization of Ni_5B_2 can occur, then the latent heat delivered is large enough to increase the temperature of the undercooled melt. Two types of behaviour are possible according to the temperature difference between the decomposition temperature (T_d) of Ni_5B_2 and the minimum temperature (T_m) reached during cooling before recalescence for the studied composition.

If the temperature interval ($T_m - T_d$) is large enough (B = 25 at %), the increase of temperature during recalescence is not sufficient to go beyond the stability domain of Ni_5B_2. The microstructure of the sample appears as a large dendritic Ni_5B_2 globular structure (Fig. 10). After the crystallization of large numbers of Ni_5B_2 crystals, the solidification ends with the solidification of the remaining nickel.

On the contrary, if the temperature interval ($T_m - T_d$) is not very large (B = 19 at %), the latent heat release from the solidification of Ni_5B_2 (Fig. 7) is sufficient to increase the temperature of the melt beyond the stability domain of Ni_5B_2. The crystallization then continues with the solidification of a eutectic structure between nickel and Ni_3B (o) (Fig. 8) as expected from the binary diagram.

4.2.2. Preferred orientation of the ribbon

As shown by different authors [28] the melt-spinning technique results in ribbons which may have a preferred orientation which is related to the thermal gradient being perpendicular to the contact surface. The degree of preferred orientation depends essentially on the crystallographic structure of the material, and can vary from strong to none. In Ni–25 at % B alloy, preferred orientations are observed in the plane of the ribbon surface. The two main orientations are $\langle 0\,1\,0 \rangle$ and $\langle 1\,1\,0 \rangle$, but the c-axis in Ni_3B zone as well as in Ni_5B_2 zone is always found parallel to the surface of the ribbon indicating strong relationship between thermal gradient and the formation of pleated metal atom layers in the two crystalline structures.

4.2.3. Behaviour at the eutectic composition

Solidification of slowly cooled lamellar eutectic has been extensively studied. The results agree with the theoretical model developed by Jackson and Hunt [29]. Two assumptions are used:

(i) the lamellar spacing (λ) is smaller than the diffusion distance D/V where D is the diffusion coefficient of the solute in liquid and V the solidification velocity,

(ii) the undercooling (ΔT) is small.

At low solidification velocities, $\lambda^2 V = a/b$ and $\Delta T/V = 4ab$ remain constant; a and b are calculated from physical properties in the binary system. But under rapid solidification and high solidification velocities, ΔT can be quite large and D/V small. The model was extended recently by Trivedi *et al.* [30]. The parameters $\lambda^2 V$ and $\Delta T/V$ calculated, deviate from constant values. The numerical values for the Ni–B system are listed in Table III.

The lamellar spacing (λ) decreases with increasing cooling rate but is not inversely proportional to the growth rate as expected from the relation $\lambda^2 V = a/b$.

TABLE III Parameters used in calculations of lamellar distance (λ) and undercooling (ΔT) in Ni–Ni_3B eutectic

Eutectic temperature, T_e (K)	1383
Distribution coefficient of boron in melt, k	0.002
Diffusion coefficient, D	2×10^{-9} m^2 sec^{-1}
Surface tension between nickel and Ni_3B, σ	0.8 J m^{-2}
Heat of fusion of nickel, ΔH	2.6×10^9 J m^{-3}
Heat of fusion of Ni_3B, ΔH	3×10^9 J m^{-3}
	$a = 1.6\,\mu$m k
	$b = 1.6 \times 10^{-2}$ k sec μm^{-2}

At high cooling rate, λ seems to be independent of the cooling rate. As previously observed by Liu and Fredriksson [31] on similar systems (Fe–Fe_3C), the volume fraction of nickel phase decreases with the cooling rate from 0.5 in as-cast or slowly cooled eutectic alloys [11] to 0.3 in melt-spun alloys.

Large undercoolings are expected due to the very small partition coefficient ($k = 0.002$) of boron in nickel. From the extension of the Ni_5B_2 domain (Fig. 14), an undercooling ΔT of 600 K for the eutectic composition is estimated which corresponds to a solidification velocity of 1 m sec^{-1}. This value is much larger than that calculated (4 cm sec^{-1}) from Newtonian heat transfer [24]

$$V = h(T_1 - T_0)/\Delta H$$

where $T_1 - T_0$ is the temperature difference between the melt, T_1, and the substrate, T_0, and ΔH is the latent heat per unit volume of the melt. This discrepancy indicates, as observed by different authors [24, 32], that for large undercooling, the solidification velocity depends only to a limited extent on external conditions.

5. Conclusion

The microstructure at a high-resolution level (HREM and EELS) and the solidification behaviour at the macroscopic level of a series of Ni–B alloys quenched by melt-spinning have been examined. A variety of microstructures were observed depending on the boron composition and on the substrate velocity. The microstructures are related to the solidification behaviour and the heat flow in undercooled melt. The solidification path of different alloys and the various morphologies are directly related to the local cooling rate.

A metastable phase was observed. The nature and the domain of the new metastable phase Ni_5B_2 of Fe_5C_2 type has been discussed. The stability domain of this phase extends from 16 to 30 at % B and decomposes at temperatures above 600° C. Furthermore, it has been shown that solid-phase precipitation occurs in the nickel phase. These precipitates are not the Ni_3B or Ni_2B phases but the very boron-rich binary compound Ni_4B_3 (o).

References

1. O. KNOTEK and E. LUGSCHEIDER, *J. Vac. Sci. Technol.* **11** (1974) 798.
2. H. T. STEINE and W. SIMM, *Int. J. Powder Metall. Powder Technol.* **18** (1982) 57.
3. S. LEBAILI and S. HAMAR-THIBAULT, *Mem. Sci. Rev. Met.* **81** (1984) 519.
4. K. I. PORTNOI, V. M. ROMASOV, V. M. CHUBAROV, M. Kh. LEVINSKAYA and S. E. SALIBEKOV, *Poroshkovaya Metallurgiya* **50** (1967) 15.
5. R. W. WYCKOFF, "Crystal Structures" (Interscience, London, 1964) Ch. VB, p. 114.
6. H. J. GOLDSMITH, "Intersticial Alloys" (Butterworths, London, 1967).
7. P. T. KOLOMYTSEV, *Izv. An. SSSR Otd. Khim. N. Met. i Toplivo* **3** (1960) 83.
8. S. RUNDQVIST, *Acta Chem. Scand.* **12** (1958) 658.
9. A. S. SCHÖBEL and H. H. STADELMAIER, *Z. Metallkde* **56** (1965) 856.
10. A. S. SOBOLEV and T. F. FEDOROV, *Izv. Akad. Nauk SSSR Neorgan. Materially* **4** (1967) 723.
11. J. AJAO and S. HAMAR-THIBAULT, *J. Mater. Sci.* **23** (1988) 1112.
12. K. SUZUKI, T. FUKUNAGA, F. ITOH and N. WATANABE, in "Rapidly Quenched Metals", edited by S. Steeb and H. Warlimont (North Holland Elsevier, London, 1985) p. 479.
13. P. CASANOVA, J. C. JOUD and C. SENILLOU, *Mem. Sci. Rev. Met.* **81** (1984) 553.
14. J. DESSEAUX-THIBAULT, "Microscopie Electronique en Sciences des Matériaux" (CNRS, 1981) Ch. XIII, p. 257-66.
15. J. M. COWLEY, "Electron Diffraction", (North Holland Elsevier, London, 1975).
16. J. DESSEAUX-THIBAULT and S. HAMAR-THIBAULT, *Sur. Interface Anal.* **9** (1985) 175.
17. N. ZALUZEC, "An Electron Energy Loss Library", (Argonne Laboratory, 1984).
18. D. G. MORRIS, *Acta Metall.* **32** (1984) 837.
19. S. NAGAKURA, J. SUZUKI and M. KUSUNOKI, *Trans. J. Inst. Metals* **22** (1981) 699.
20. J. P. SENATEUR and R. FRUCHART, *C.R.A.S. Paris* **256** (1963) 3114.
21. J. M. GENIN, G. LE CAER and A. SIMON, Proceedings of the 5th International Conference on Mössbauer Spectroscopy, Prague, Vol. 2 (1973) p. 318.
22. M. AUDIER, P. BOWEN and W. JONES, *J. Cryst. Growth* **64** (1983) 291.
23. H. JONES, "Rapid Solidification of Metals and Alloys", Institution of Metallurgists, Monographs 8 (London 1982).
24. W. J. BOETTINGER, in "Rapidly Solidified Amorphous and Crystalline Alloys", edited by B. H. Kear, R. Giessen and R. Cohen (North Holland, Elsevier, London, 1982) p. 15.
25. T. W. CLYNE and A. GARCIA, *J. Mater. Sci.* **16** (1981) 1643.
26. H. FREDRIKSSON, A. OLSTHUD and H. SODERHJELM, in "Rapidly Quenched Metals", edited by Steeb, H. Warlimont, (North Holland Elsevier, Wurtsburg, 1984) p. 187.
27. R. SELLGER and W. LÖSER, *Acta Metall.* **34** (1986) 831.
28. N. W. BLAKE, F. A. HAMES and R. W. SMITH, in "Rapidly Solidified Amorphous and Crystalline Alloys", edited by B. H. Kear, R. Giessen and R. Cohen (North Holland, Elsevier, London, 1982) p. 363.
29. J. D. HUNT and K. A. JACKSON, *Trans. AIME* **236** (1966) 843.
30. R. TRIVEDI, P. MAGNIN and W. KURZ, *Acta Metall.* **35** (ASME, London, 1987) 971.
31. J. LUI and H. FREDRIKSSON, International Conference on Solidification Processing, Sheffield (1987) p. 245.
32. A. LASALMONIE and F. DUFLOS, in "Solidification des alliages", edited by F. Durand (Ed. de Physique, Paris, 1988) p. 313.

Received 22 June
and accepted 8 December 1988